cancers

MDPI

Article

Mitochondrial ROS1 Increases Mitochondrial Fission and Respiration in Oral Squamous Cancer Carcinoma

Yu-Jung Chang [1,*], Kuan-Wei Chen [1] and Linyi Chen [1,2,*]

[1] Institute of Molecular Medicine, National Tsing Hua University, Hsinchu 30013, Taiwan; kwchen@gate.sinica.edu.tw

[2] Department of Medical Science, National Tsing Hua University, Hsinchu 30013, Taiwan

* Correspondence: ddcarol18@gapp.nthu.edu.tw (Y.-J.C.); lchen@life.nthu.edu.tw (L.C.); Tel.: +886-3-571-5131#33473 (Y.-J.C.); +886-3-574-2775 (L.C.); Fax: +886-3-571-5934 (L.C.)

Received: 7 July 2020; Accepted: 30 September 2020; Published: 1 October 2020

Simple Summary: The clinical efficacy of anti-epidermal growth factor receptor (EGFR) antibody cetuximab for oral squamous cell carcinomas (OSCCs) is low. We previously reported that an increased oncogenic ROS proto-oncogene 1 (ROS1) is responsible for the invasiveness and metastasis of OSCC. This study demonstrates for the first time that ROS1, a receptor tyrosine kinase, can localize to mitochondria. Mitochondrial ROS1 in the highly invasive OSCC promotes mitochondrial fission, enhances mitochondrial oxidative phosphorylation and ATP production but reduces mitochondrial biogenesis. These findings highlight the novel function of ROS1 in mitochondrial morphogenesis and metabolic adaptation to promote OSCC invasiveness.

Abstract: Increased ROS proto-oncogene 1 (ROS1) expression has been implicated in the invasiveness of human oral squamous cell carcinoma (OSCC). The cellular distribution of ROS1 has long-been assumed at the plasma membrane. However, a previous work reported a differential cellular distribution of mutant ROS1 derived from chromosomal translocation, resulting in increased carcinogenesis. We thus hypothesized that cellular distribution of upregulated ROS1 in OSCC may correlate with invasiveness. We found that ROS1 can localize to mitochondria in the highly invasive OSCC and identified a mitochondria-targeting signal sequence in ROS1. We also demonstrated that ROS1 targeting to mitochondria is required for mitochondrial fission phenotype in the highly invasive OSCC cells. OSCC cells expressing high levels of ROS1 consumed more oxygen and had increased levels of cellular ATP levels. Our results also revealed that ROS1 regulates mitochondrial biogenesis and cellular metabolic plasticity. Together, these findings demonstrate that ROS1 targeting to mitochondria enhances OSCC invasion through regulating mitochondrial morphogenesis and cellular respiratory.

Keywords: *ROS1* oncogene; mitochondrial fission; mitochondrial respiratory capacity; oral cancer

1. Introduction

Oral cancer is the sixth-most-common cancer worldwide, and approximately 90% of oral cancers are oral squamous cell carcinomas (OSCCs). Unfortunately, most patients with oral cancer are diagnosed at an advanced stage with neck lymph-node metastasis [1]. The monoclonal antibody therapeutic cetuximab, which targets epidermal growth factor receptor (EGFR), is the most commonly prescribed treatment for advanced OSCC [2], although its clinical efficacy is limited [3,4] owing to drug resistance or lack of response [5]. Therefore, understanding the molecular mechanisms underlying OSCC metastasis is essential for designing more effective therapeutic approaches.

Receptor tyrosine kinases (RTKs) are synthesized in the endoplasmic reticulum, delivered to the Golgi, and then targeted to the plasma membrane as single-transmembrane proteins where they transduce extracellular signals to orchestrate diverse physiological responses [6]. The *ROS proto-oncogene 1 (ROS1)* encodes an RTK containing a large N-terminal extracellular domain, a single-transmembrane domain, and an intracellular, C-terminal tyrosine kinase domain. We previously showed that upregulation of *ROS1* oncogene leads to oral cancer metastasis [7]. The highly invasive OSCC lines, OC3-IV2 and C9-IV2, express increased levels of ROS1. These two cell lines were in-vivo selected, highly invasive cells [7,8]. In addition, genomic rearrangements in the *ROS1* gene have been implicated in cancer progression [9]. Unlike ROS1 which has been assumed to localize at the plasma membrane [10], ROS1 fusion proteins derived from chromosomal translocations exhibit differential subcellular localizations and their oncogenic potential can vary. For example, in glioblastoma, the FIG-ROS1 oncoprotein containing a Golgi-targeting signal, targets to the Golgi rather than the plasma membrane resulting in oncogenic transformation [11]. Similarly, the endosome-localized fusion proteins SDC4-ROS1 and SLC34A2-ROS1 and endoplasmic reticulum-localized fusion protein CD74-ROS1 differentially activate mitogen-activated protein kinase (MAPK) [12]. These findings suggest that subcellular distribution of ROS1 may determine its oncogenic properties. To address this issue, we examined the subcellular localization of ROS1—the results provide new insight into the role of ROS1 in regulating OSCC invasiveness.

2. Results

2.1. ROS1 Is Present in Mitochondria

To determine the subcellular localization of ROS1, immunofluorescence staining of ROS1 was performed. ROS1 distribution in C9-IV2 cells was found mainly in the cytoplasm (Figure 1A). ROS1 is an RTK—it is not surprising that ROS1 could transit the endoplasmic reticulum during its normal translocation to the plasma membrane. Our unexpected findings were their colocalization with mitochondrial outer membrane protein TOM20 (Figure 1A). The color map of ROS1 and mitochondrial colocalization was generated using the nMDP value, and the Icorr was calculated using the Colocalization Colormap plugin of ImageJ (Figure 1A, right bottom panel). Icorr indicated significant colocalization of ROS1 with mitochondria (Icorr = 0.717). Confocal images of COS7 cells overexpressing ROS1-myc also showed significant distribution of ROS1 to mitochondria (Icorr = 0.811; Figure 1B). The fact that Cheng and colleagues reported higher expression of ROS1 in the cytoplasm of OSCC tissues than that in the adjacent dysplastic, epithelial tissues suggests that the subcellular localization of ROS1 may be involved in disease progression [13]. We next used biochemical fractionation of the highly invasive OSCC cell line OC3-IV2 to confirm the subcellular location of ROS1, revealing that ROS1 was indeed present in both the mitochondrial and cytosolic fractions (Figure 1C). Similarly, the localization of ROS1-myc in 293T cells transfected with an ROS1-myc construct was examined using biochemical fractionation; ROS1-myc was distributed to both mitochondria and cytosol (Figure 1D). To examine the submitochondrial locale of ROS1, the mitochondrial fractions collected from OC3-IV2 cells were subjected to digestion with proteinase K. ROS1 and TOM20 were digested similarly by proteinase K at 0.5 to 2 μg/mL, whereas the mitochondrial inner membrane protein TIM23 remained protected, suggesting that ROS1 is likely a mitochondrial outer membrane protein. As a positive control, triton X-100 treatment disrupted the membrane allowing access of proteinase K to digest TIM23 (Figure 1E).

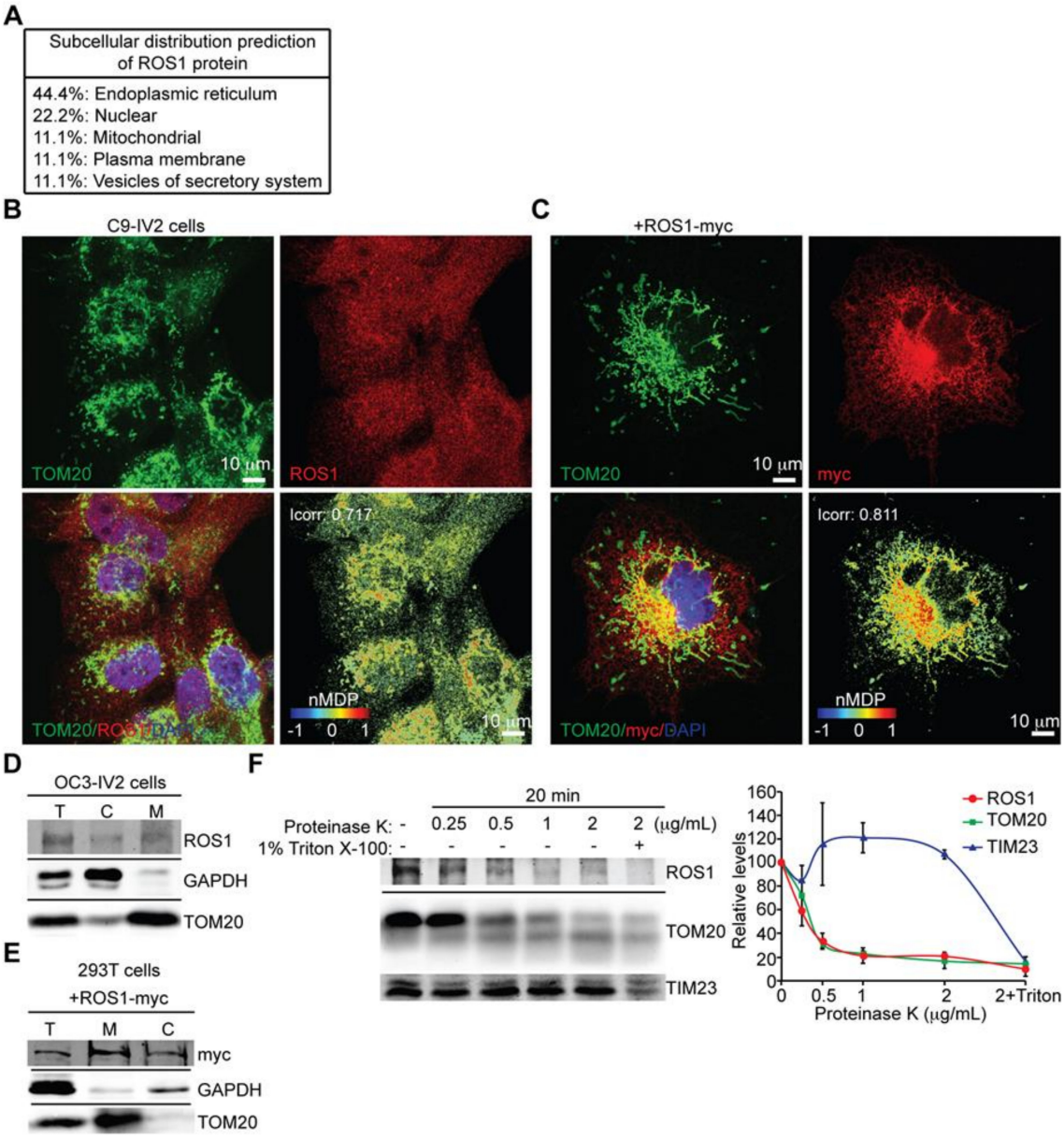

Figure 1. Mitochondrial localization of ROS proto-oncogene 1 (ROS1). (**A**) C9-IV2 cells were subjected to immunostaining for endogenous ROS1 (red) and TOM20 (mitochondria, green) together with 4′,6-diamidino-2-phenylindole (DAPI) (nucleus, blue). Colocalization Colormap images of ROS1 and TOM20 (bottom right panel) was shown in the normalized mean deviation product (nMDP) value. nMDP value: range 0 to 1, colocalization (warm colors); range −1 to 0, noncolocalization (cold colors). Icorr, index of correlation. (**B**) COS7 cells transfected with ROS1-myc were subjected to immunostaining for myc (red) and TOM20 (green) together with DAPI (blue). Colocalization Colormap images are shown in the bottom right panel. (**C**) Subcellular fractionation of OC3-IV2 cells followed by immunoblotting with anti-ROS1, anti-GAPDH, and anti-TOM20. GAPDH and TOM20 served as markers of the cytoplasm and mitochondria, respectively. T: total cell lysate, C: cytoplasmic fraction, M: mitochondrial fraction. (**D**) Mitochondria and cytosol were subjected to subcellular fractionation of 293T cells transfected with ROS1-myc. Proteins were analyzed by immunoblotting for ROS1, GAPDH, and TOM20. (**E**) Mitochondria isolated from OC3-IV2 cells were treated with various concentrations of proteinase K for 20 min. Isolated mitochondria that were treated with both proteinase K and Triton X-100 (1%) served as the positive control. Proteins were analyzed by immunoblotting for ROS1, TOM20,

and TIM23. The right curve plot shows the relative protein level for ROS1, TOM20, and TIM23 after treatment with different concentrations of proteinase K. Proteins were quantified and normalized to the amounts in the no-treatment control. Data from three independent experiments are presented as mean ± SEM. Scale bar: 10 μm in (**A**,**B**).

2.2. ROS1 Contains a Novel Mitochondria-Targeting Signal

Based on the immunostaining and biochemical fractionation results for ROS1 distribution in mitochondria, we next determined which region of ROS1 is responsible for mitochondria targeting. Mitochondrial proteins that are encoded by nuclear genes contain both a moderately hydrophobic transmembrane (T) domain with positively charged residues (P) that flank the T domain and target the proteins to mitochondria [14]. In addition to the three well-defined regions of ROS1, namely the N-terminal extracellular region, T domain, and C-terminal kinase domain, we discovered that the T domain is hydrophobic with a basic, positively charged flanking region (residues 1883–1894, defined as the P region; Figure 2A, left panel). To determine whether the TP segment of ROS1 constitutes a functional mitochondria-targeting signal, we attached GFP to the C-terminus of the TPC region [ROS1(TPC)-GFP], T alone [ROS1(T)-GFP], TP segment [ROS1(TP)-GFP], the PC region [ROS1(PC)-GFP], or C-terminal kinase domain alone [ROS1(C)-GFP] (Figure 2A, right panel). 293T cells were transfected with these mutant constructs individually, and their expression was confirmed by immunoblotting (Figure 2B).

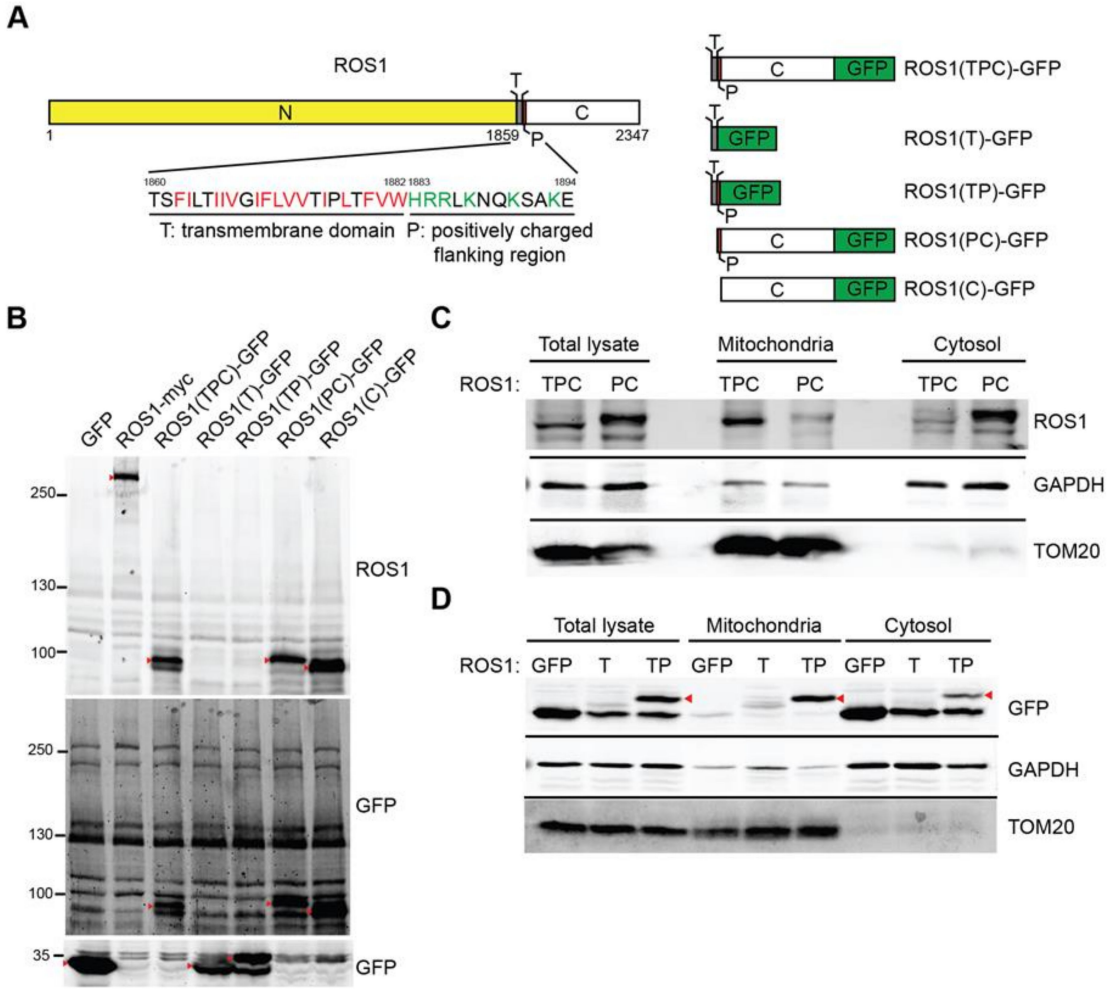

Figure 2. Identification of a mitochondrial targeting sequence in ROS1. (**A**) Schematic representation

of ROS1 mutants. N, N-terminal region; T, transmembrane domain (hydrophobic residues, red); P, positively charged flanking region (positively charged residues, green); C, C-terminal kinase domain. (**B**) 293T cells were transiently transfected with GFP, ROS1-myc, ROS1(TPC)-GFP, ROS1(T)-GFP, ROS1(TP)-GFP, ROS1(PC)-GFP, or ROS1(C)-GFP. Cell lysates were resolved via SDS-PAGE followed by immunoblotting with anti-ROS1 and anti-GFP. Red arrowheads indicate the proteins of interest. (**C**) 293T cells were transiently transfected with ROS1(TPC)-GFP or ROS1(PC)-GFP, fractionated, and immunoblotted with anti-ROS1, anti-GAPDH, and anti-TOM20. (**D**) Mitochondrial and cytosol fractions of 293T cells transfected with GFP, ROS1(T)-GFP, or ROS1(TP)-GFP were subjected to subcellular fractionation. Proteins were analyzed by immunoblotting for ROS1, GAPDH, and TOM20.

To investigate whether the hydrophobic T domain is required for mitochondrial delivery, 293T cells were transfected with the ROS1(TPC)-GFP or ROS1(PC)-GFP constructs, and the localization of the expressed ROS1(TPC) or ROS1(PC) was determined by subcellular fractionation. A significant amount of ROS1(TPC) was present in the mitochondrial fractions (Figure 2C), whereas ROS1(PC) was primarily detected in the cytosol. This finding suggests that the hydrophobic T domain of ROS1 is important for mitochondrial targeting. To further examine whether the flanking P region of the T domain contributes to ROS1 localization to the mitochondria, we analyzed the localization of GFP, ROS1(T)-GFP, and ROS1(TP)-GFP. Figure 2D showed that the TP region of ROS1 was able to bring GFP protein into the mitochondria, whereas the T domain alone cannot, suggesting that the P region is required for ROS1 localization to mitochondria. These results indicated that the TP region of ROS1 constitutes a functional mitochondria-targeting signal.

2.3. Mitochondria are More Fragmented in Highly Invasive Oral Cancer Cells

We previously reported that epigenetically upregulated ROS1 expression increased cancer invasiveness and led to OSCC metastasis [7]. The fact that significant parts of ROS1 localized to mitochondria (Figure 1) and cancer metastasis was linked to dysregulated mitochondrial morphogenesis [15,16], we next investigated whether mitochondrial ROS1 could enhance OSCC invasiveness by affecting mitochondrial morphogenesis. To this end, we compared the mitochondrial morphology of isogenic pairs of the highly invasive OSCC cell lines OC3-IV2 and C9-IV2 to that of their respective parental lines, OC3 and C9 cells. Immunofluorescence staining and confocal microscopy for TOM20 were used to monitor mitochondrial morphology. Mitochondria were more elongated and tubular in OC3 cells, whereas they were highly fragmented in OC3-IV2 cells and some of the OC3-IV2 mitochondria were of intermediate length (Figure 3A,B). Similarly, C9-IV2 cells contained more fragmented mitochondria than C9 cells (Figure 3C,D). Here, we linked mitochondrial ROS1, fragmented mitochondria, and OSCC invasiveness.

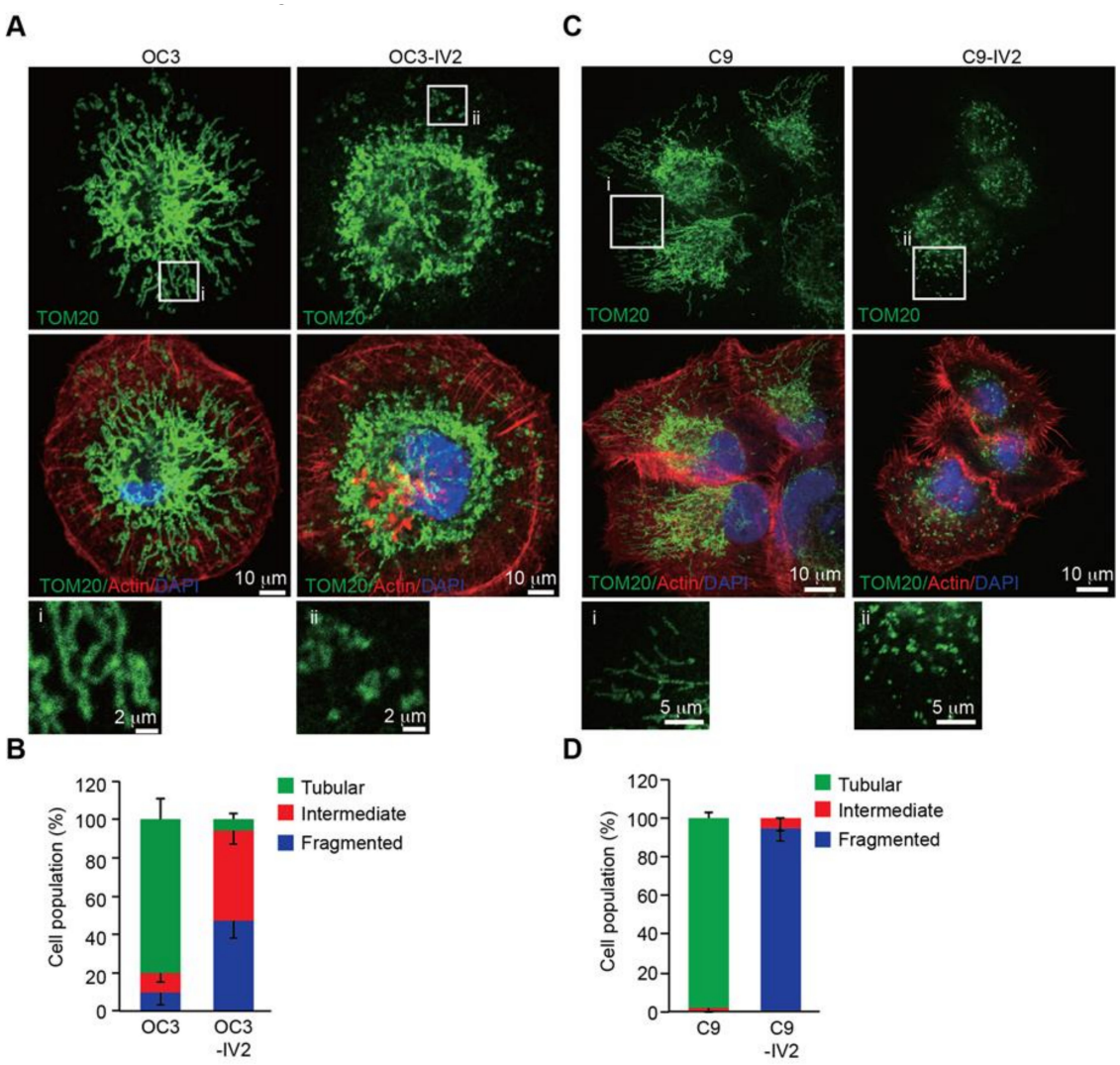

Figure 3. Mitochondria are fragmented in the highly invasive OSCC cells. (**A–D**) OC3 and OC3-IV2 (**A**) or C9 and C9-IV2 cells (**C**) were subjected to immunostaining using anti-TOM20 (green), rhodamine phalloidin (actin, red), and DAPI (nucleus, blue). Enlarged panels from the boxed area are shown in the bottom panel. (**B**,**D**) Assessment of mitochondrial morphology in cell lines OC3 (n = 68 cells), OC3-IV2 (n = 120 cells), C9 (n = 22 cells), and C9-IV2 (n = 30 cells) in (**A**,**C**). Data from at least three independent experiments are presented as mean ± SEM. Scale bar: 10 μm (A and C); 2 μm (**A**), and 5 μm (**C**) for enlarged images.

2.4. ROS1 Expression Induces Mitochondrial Morphogenesis in OSCC Cells

Inhibition of ROS1 activity results in reduced cell proliferation, migration, and invasion of OSCC cells [7], so we investigated whether suppression of ROS1 activity could block mitochondrial fission. We treated C9-IV2 cells with DMSO or foretinib (ROS1 inhibitor) and assessed mitochondrial morphology. Foretinib dramatically decreased mitochondrial fission in C9-IV2 cells compared to treatment with DMSO (Figure 4A,B).

To determine whether mitochondrial fragmentation of highly invasive OSCC cells occurred in an ROS1-dependent manner, the morphology of mitochondria in OC3-IV2 cells stably expressing a scrambled shRNA (OC3-IV2-Scr) or ROS1-specific shRNA (OC3-IV2-shROS1) was investigated by imaging. In OC3-IV2 cells, ROS1 knockdown reversed the fragmented phenotype to produce elongated mitochondria (Figure 5A,B). In addition, overexpression of ROS1 caused the fused mitochondrial

morphology of C9 cells to become fragmented (Figure 5C,D). These data indicated that increased ROS1 and its activity were sufficient to alter mitochondrial morphology.

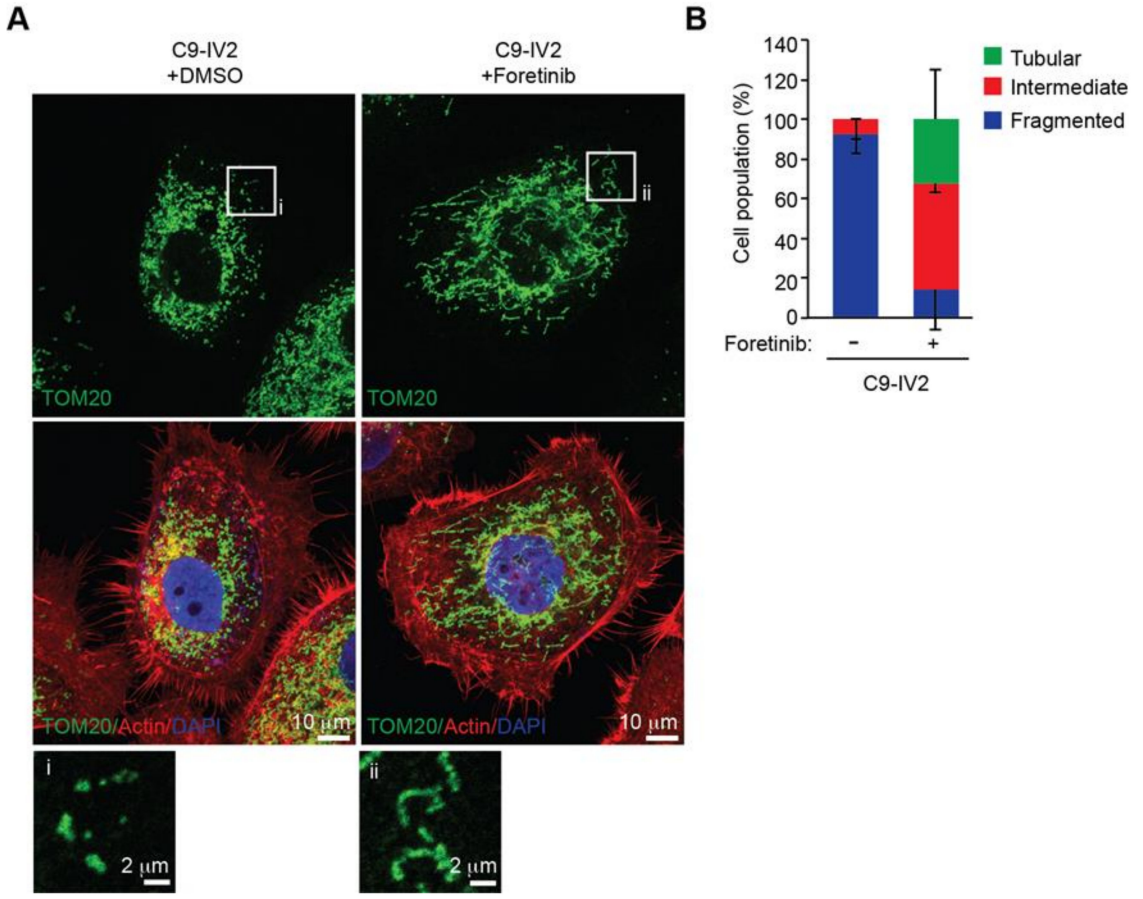

Figure 4. Inhibition of ROS1 signaling leads to mitochondrial fusion. (**A**) Assessment of mitochondrial morphologies in C9-IV2 cells treated for 24 h with DMSO or 500 nM foretinib (ROS1 inhibitor). Green, TOM20; red, actin; blue, DAPI. (**B**) Quantification of mitochondrial morphology from (**A**). Data from three independent experiments are presented as mean ± SEM. Scale bar: 10 μm (**A**); 2 μm (enlarged images).

We next determined whether the mitochondria-targeting signal of ROS1 could affect the morphogenesis of mitochondria. OC3 cells were transfected with the ROS1(TPC)-GFP or ROS1(PC)-GFP constructs and distribution and effect of each protein on mitochondrial morphogenesis were determined by immunofluorescence staining. Confocal images and positive nMDP colocalization values indicated that ROS1(TPC)-GFP localized to mitochondria to a greater extent than ROS1(PC)-GFP (Figure 6A,B). In addition, mitochondria were elongated and tubular in OC3 cells transfected with GFP or ROS1(PC)-GFP, whereas they were mainly fragmented in cells transfected with ROS1(TPC)-GFP (Figure 6A,C). Transfection of COS7 cells with the full-length ROS1 or ROS1-truncated mutant ROS1(TPC) (containing the T domain with the P region) revealed mitochondrial localization of each protein and fragmented mitochondria, whereas this was not the case for COS7 cells transfected with ROS1(PC) (Figure S1). These results indicated that the newly identified mitochondria-targeting signal is required for mitochondrial delivery of ROS1 and promotes mitochondrial fission.

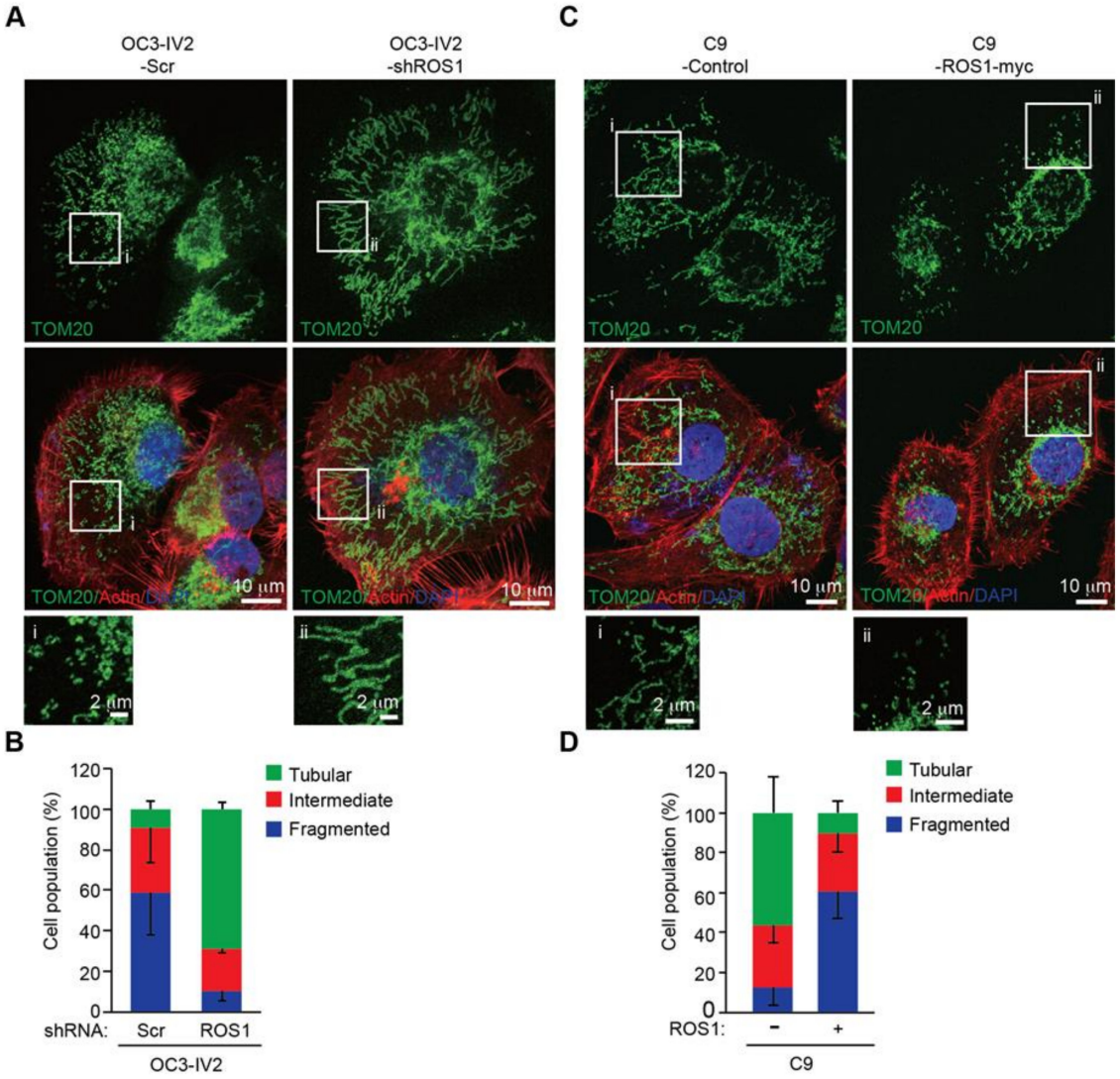

Figure 5. Oncogenic ROS1 is sufficient for mitochondrial fragmentation. (**A**) OC3-IV2 cells stably expressed an shRNA-targeting ROS1 mRNA (OC3-IV2-shROS1) or a scrambled/control shRNA (OC3-IV2-Scr). Mitochondrial morphology was analyzed by immunostaining: green, TOM20; red, actin; blue, DAPI. (**B**) Quantification of mitochondrial morphology in cell lines OC3-IV2-Scr (n = 40 cells) and OC3-IV2-shROS1 (n = 35 cells). Data from two independent experiments are presented as mean ± SD. (**C**) Representative images of the mitochondrial morphologies observed in C9 cells stably transfected with vector only (C9-control) or human ROS1 cDNA (C9-ROS1-myc). Green, TOM20; red, actin; blue, DAPI. (**D**) Quantification of the mitochondrial morphologies observed in the cells shown in (**C**). Data in (**D**) represent the mean ± SEM of three independent experiments with C9-control (n = 32 cells) and C9-ROS1-myc (n = 51 cells). Scale bar: 10 μm (**A**,**C**); 2 μm (enlarged images in **A** and **C**).

2.5. ROS1 Enhances Mitochondrial Bioenergetics and Metabolic Plasticity but Reduces Mitochondrial Biogenesis in OSCC Cells

The dynamics of mitochondrial morphogenesis correlate with changes in bioenergetics, cell metabolism, and motility [17]. To determine the physiological implications of mitochondrial morphogenesis, we measured the mitochondrial oxygen consumption rate (OCR) and ATP synthesis in OC3 and OC3-IV2 cells. The fraction of basal OCR inhibited by the ATP synthase inhibitor oligomycin was used to estimate the mitochondrial respiration rate required to sustain cellular ATP production. The protonophoric uncoupler carbonyl cyanide-4-(trifluoromethoxy)phenylhydrazone (FCCP) stimulates the mitochondrial electron transport system to function at its maximal capacity,

defined as maximal OCR. The spare respiratory capacity is the difference between the basal and maximal OCR in response to a stress. Antimycin A and rotenone inhibit the mitochondrial electron transport system through Complexes I and III to allow measurement of nonmitochondrial respiration processes. The basal OCR was not significantly different between OC3 and OC3-IV2 cells. OC3-IV2 cells, on the other hand, exhibited a 55% enhancement of maximal OCR, a 2-fold elevation in spare respiratory capacity, and a 30% increase in ATP production compared to OC3 cells (Figure 7A,B), reflecting higher energy production in OC3-IV2 cells. This result revealed a link between spare respiratory capacity, ATP production, and cell invasiveness. To examine whether ROS1 directly regulates mitochondrial bioenergetics, we knocked down ROS1 in OC3-IV2 cells and determined the effect on mitochondrial OCR. Compared to control OC3-IV2-Scr cells, knockdown of ROS1 reduced basal OCR, maximal OCR, spare respiratory capacity, and ATP production (Figure 7C,D). These results demonstrated that elevated ROS1 enhances mitochondrial bioenergetics.

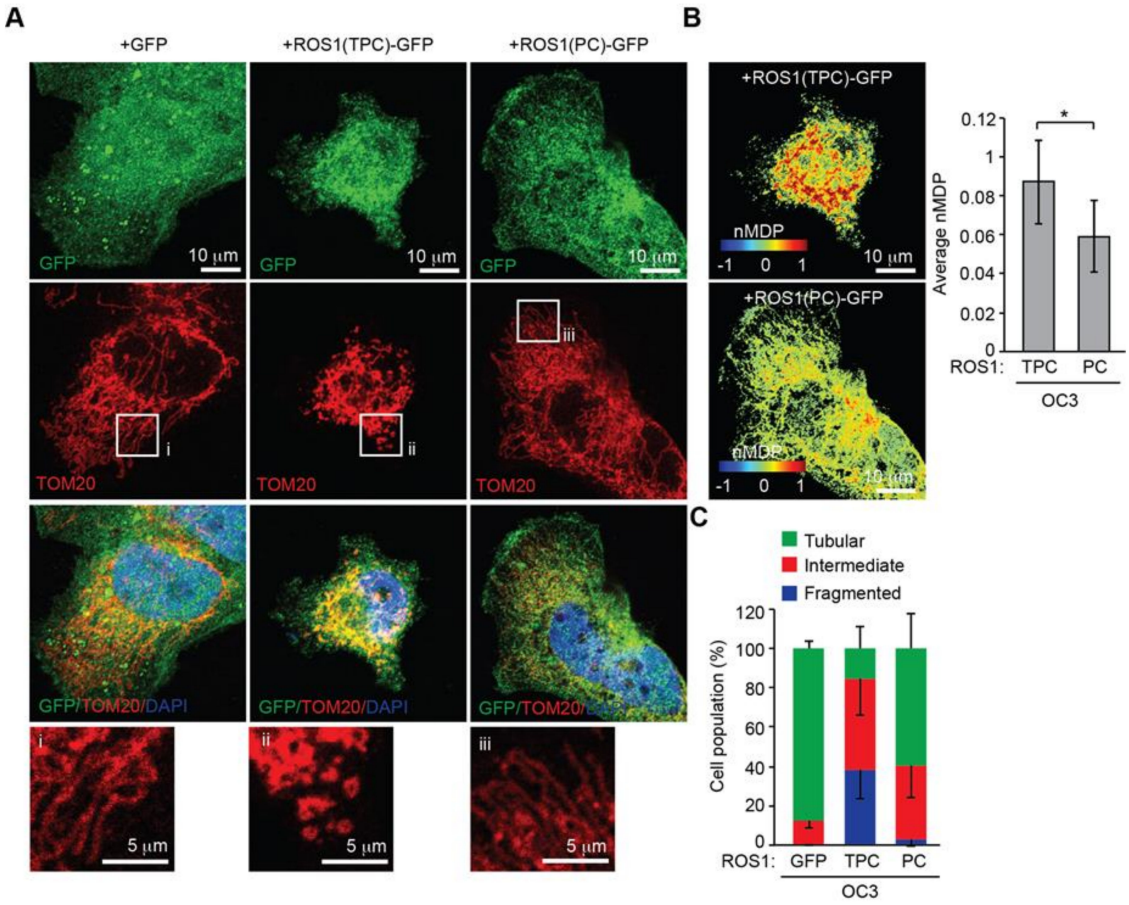

Figure 6. The TP domain of ROS1 is important for ROS1 localization to mitochondria and for ROS1-mediated mitochondrial fragmentation. (**A**) OC3 cells were transfected with a vector expressing GFP, ROS1(TPC)-GFP, or ROS1(PC)-GFP, and were then immunostained with anti-TOM20 (mitochondria, red) antibody and DAPI (nucleus, blue). (**B**) Colocalization Colormap images of ROS1 mutants and TOM20 as described in (**A**). The average of all positive nMDP values represents the abundance of ROS1 mutants in mitochondria. (**C**) Assessment of mitochondrial morphology in OC3 cells transfected with GFP (n = 39 cells), ROS1(TPC)-GFP (n = 25 cells), or ROS1(PC)-GFP (n = 24 cells) described in (**A**). Data from at least three independent experiments are presented as mean ± SEM (* $p < 0.05$, paired Student's t-test). Scale bar: 10 μm (**A**,**B**); 5 μm (enlarged images in **A**).

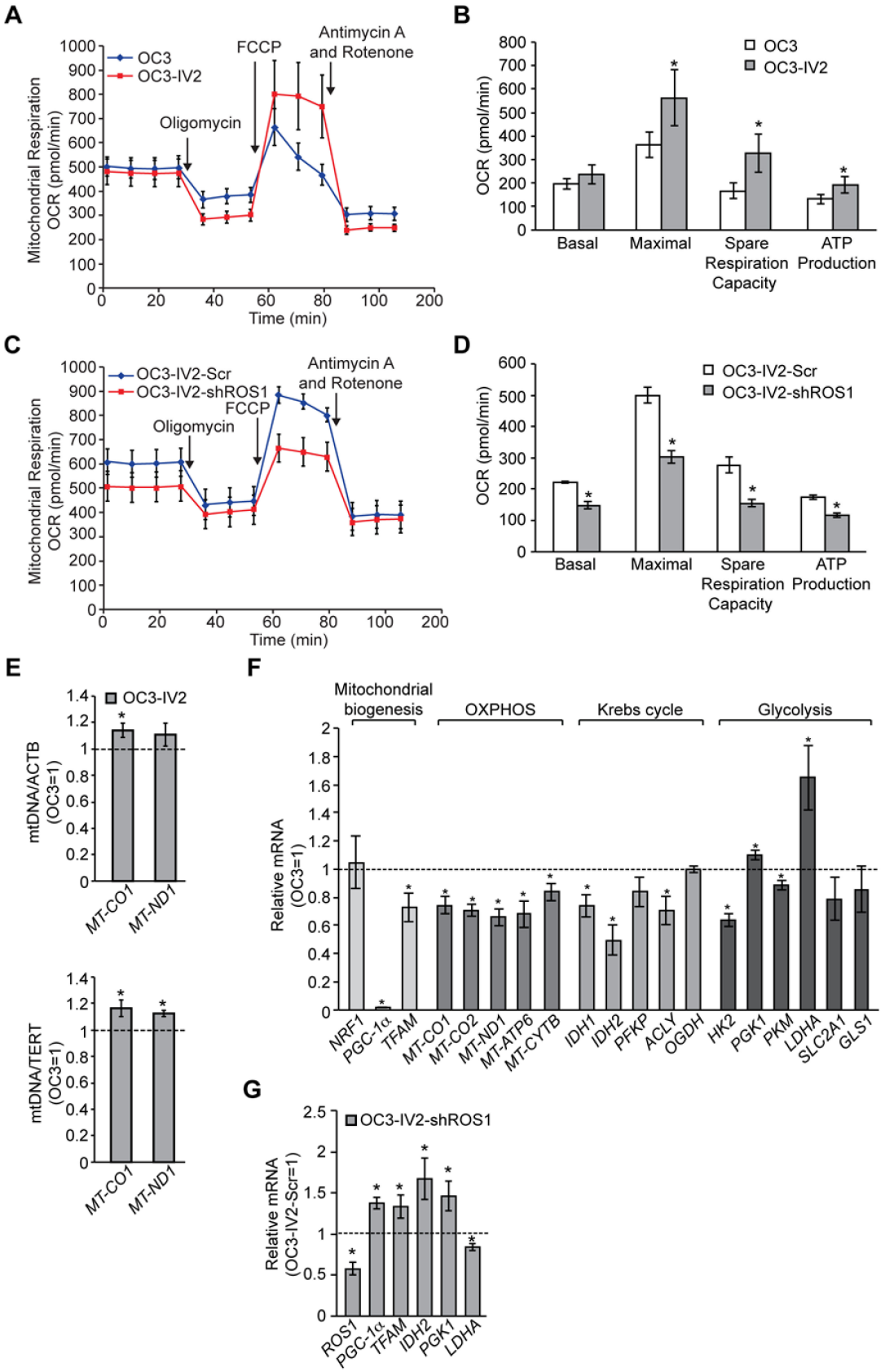

Figure 7. ROS1 affects mitochondrial function in OSCC cells. (**A–D**) Measurement of oxygen consumption rate (OCR) in OC3 and OC3-IV2 (**A**) or OC3-IV2-Scr and OC3-IV2-shROS1 cells (**C**) using

the Seahorse XF24 analyzer. (**B**,**D**) Average basal OCR, maximal OCR, spare respiration capacity, and ATP production in OC3 and OC3-IV2 (**B**) or OC3-IV2-Scr and OC3-IV2-shROS1 cells (**D**) are shown. (**E**) The relative mtDNA content was measured by Q-PCR. The expression of *MT-CO1* or *MT-ND1* was normalized to nuclear-encoded *ACTB* or *TERT* from OC3 and OC3-IV2 cells. (**F**) Q-PCR of the mRNA levels of the indicated genes in OC3-IV2 cells normalized to that of OC3 cells. Genes were grouped into functional clusters related to mitochondrial biogenesis, OXPHOS, Krebs cycle, and glycolysis. (**G**) The mRNA levels of the indicated genes in OC3-IV2-shROS1 cells were normalized to those measured in OC3-IV2-Scr. Data from three independent experiments are presented as mean ± SEM (* $p < 0.05$, paired Student's *t*-test).

It is possible that ROS1-dependent enhancement of mitochondrial bioenergetics may be due to increased mitochondrial biogenesis. To study this issue, we measured the mitochondrial DNA content and expression of genes associated with mitochondrial oxidative phosphorylation (OXPHOS) and mitochondrial biogenesis. OC3-IV2 cells had higher mitochondrial DNA content, whereas the expression of mitochondrial protein-coding genes of the OXPHOS system, namely *MT-CO1*, *MT-CO2*, *MT-ND1*, *MT-ATP6*, and *MT-CYTB*, was reduced in OC3-IV2 cells compared to OC3 cells (Figure 7E,F). Expression of the transcriptional cofactor *PGC-1α* and the master transcription factor *TFAM* for biogenesis was also downregulated in OC3-IV2 cells (Figure 7F). These data indicated that OXPHOS and ATP production in highly invasive oral cancer cells are concomitant with lower mitochondrial biogenesis. In addition, *PGC-1α* and *TFAM* expressions increased when ROS1 was reduced (Figure 7G), implicating a direct role for ROS1 in modulating mitochondrial biogenesis.

As efficient mitochondrial OXPHOS has been implicated in cellular metabolism [18], we investigated the effects of the ROS1-induced increase in mitochondrial bioenergetics on expression of genes encoding metabolic enzymes. Compared to OC3 cells, we found that the expression of genes associated with the Krebs cycle and glycolysis, including *IDH1*, *IDH2*, *ACLY*, *HK2*, and *PKM*, was reduced in OC3-IV2 cells, whereas *PGK* and *LDHA* were upregulated in OC3-IV2 cells (Figure 7F). Lactate dehydrogenase A, encoded by *LDHA*, converts pyruvate to lactate and generates ATP—and this pathway has been shown to be an essential source of energy for cancer cells [19]. We also found that ROS1 knockdown led to marked downregulation of *LDHA* (Figure 7G), suggesting that ROS1 can modulate the expression of *LDHA*. This is consistent with the idea that cancer cells maximize ATP production by both glycolysis and OXPHOS, resulting in the utilization of different nutrients and an increase in metabolic plasticity to maintain tumor survival and metastasis during different stages of disease progression [20]. Together, our findings describe a new role for the *ROS1* oncogene in enhancing mitochondrial bioenergetics and metabolic plasticity to promote OSCC invasiveness.

3. Discussion

To our knowledge, this is the first study to demonstrate the mitochondrial distribution of oncogenic ROS1. We also showed that *ROS1* oncogene upregulation in highly invasive OSCC induces mitochondrial fragmentation. Nonetheless, co-immunoprecipitation experiments revealed no interaction between ROS1 and the respective mitochondrial fission and fusion proteins dynamin-related protein 1 (DRP1) and mitofusin 2 (MFN2) (Figure S2). Although this is a negative result, it remains possible that ROS1, DRP1, or MFN2 may interact transiently at the mitochondrial outer membrane. Since ROS1 is known to activate MAPK kinase-extracellular signal-regulated kinase (ERK1/2) and phosphatidylinositol 3-kinase-AKT pathways to promote OSCC cell proliferation and invasion [7], we cannot exclude the possibility that ROS1 may regulate mitochondrial morphogenesis through ERK2 and AKT-mediated increases of DRP1 activity [21,22]. To identify candidate binding partners for ROS1, we immunoprecipitated ROS1-containing complexes, followed by two-dimensional electrophoresis and mass spectrometry. This approach identified α-enolase, which participates in stabilization of the mitochondrial membrane by binding to an integral mitochondrial membrane protein, VDAC1 [23], and protein disulfide isomerase A1, which binds to DRP1, thus reducing the activity of DRP1 and

preventing mitochondrial fission [24]. Thus, ROS1 could potentially interact with DRP1-containing complexes and regulate mitochondrial membrane remodeling.

EGFR is another RTK that undergoes subcellular trafficking from the cell surface to the nucleus, Golgi, or endoplasmic reticulum and influences transcriptional regulation, tumor progression, and drug resistance [25]. EGF-induced endocytosis of EGFR results in the translocation of EGFR to the mitochondria [26,27]. Mitochondrial EGFR also induces mitochondrial fission through inhibition of MFN1 and enhances energy production and cell motility to promote metastasis of non-small-cell lung cancer [27]. Mitochondria-localized EGFR associates with c-Src at the mitochondrial inner membrane to phosphorylate cytochrome c oxidase subunit II (COXII), a component of the complex IV of the mitochondrial electron transport system; the interaction leads to inhibition of the COXII activity and to a reduction in ATP levels in breast cancer cells [26]. ROS1 at the outer membrane may similarly interact with components in the electron transport system and regulate OCR. These examples reveal multiple functions of RTKs in regulating cancer progress through trafficking to different organelles and potentially being post-translationally modified or cleaved [28].

What is the physiological implication of the ROS1-induced increase in mitochondrial respiration? One clue from metastatic breast cancer cells is the association between mitochondrial OXPHOS and stemness [29]. We found that the stemness genes *ALDH1*, *SOX2*, and *IL13RA2* were upregulated in OC3-IV2 cells, in which *ROS1* is highly expressed (Figure S3). However, it remains unknown how ROS1 and increased mitochondrial respiration lead to the upregulation of stemness genes. On the other hand, ROS1 knockdown results in tubular mitochondria and reduced ATP production, which explains its suppression of cell growth, migration, and invasion of OSCC cells [7].

4. Materials and Methods

4.1. Reagents

Anti-ROS1 (#3266, 1:1000 for immunoblotting, 1:100 for immunofluorescence staining) and anti-DRP1 (#8570, 1:1000 for immunoblotting) antibodies were purchased from Cell Signaling Technology (Danvers, MA, USA). Anti-GAPDH (#G8795, 1:5000 for immunoblotting) and anti-myc tag (#05-724MG, 1:1000 for immunoblotting) antibodies were purchased from Sigma-Aldrich (St Louis, MO, USA). Anti-TOM20 (#sc-11415, 1:1000 for immunoblotting, 1:100 for immunofluorescence staining) and anti-TIM23 (#sc-514463, 1:1000 for immunoblotting) were purchased from Santa Cruz Biotechnology (Santa Cruz, CA, USA). Secondary antibodies conjugated to Alexa Fluor 700 (#A21036), Alexa Fluor 488 (#A11001), Alexa Fluor 555 (#A21428), or Alexa Fluor 647 (#A21235) were purchased from Invitrogen (Carlsbad, CA, USA) and diluted 1:10,000. Rhodamine phalloidin (#A12379) was purchased from Invitrogen and diluted 1:1000 for immunofluorescence staining. IRDye800CW-labeled anti-rabbit secondary antibody (#926-32211, 1:10,000 for immunoblotting) was purchased from LI-COR Biosciences (Lincoln, NE, USA). Anti-GFP tag (#GTX113617, 1:1000 for immunoblotting) and anti-mCherry (#GTX59788, 1:1000 for immunoblotting) antibodies were purchased from GeneTex (Irvine, CA, USA). Foretinib (#A2974) was purchased from ApexBio Technology (Houston, TX, USA).

4.2. Cell Culture

COS7 cells and 293T cells were obtained from the American Type Culture Collection—the human oral cancer cell lines CGHNC9 (C9), C9-IV2, OC3, and OC3-IV2 have been described [8,30,31]. OC3 and OC3-IV2 cells were maintained in a 1:1 mixture of Dulbecco's modified Eagle medium (DMEM; Invitrogen) and keratinocyte serum-free medium (Invitrogen) containing 10% *(v/v)* fetal bovine serum (Invitrogen), 1% *(v/v)* L-glutamine (Invitrogen), and 1% *(v/v)* antibiotic-antimycotic (Invitrogen) and cultured at 37 °C and 5% CO_2. C9, C9-IV2, COS7 cells, and 293T cells were maintained in DMEM with 10% *(v/v)* fetal bovine serum, 1% *(v/v)* L-glutamine, and 1% *(v/v)* antibiotic-antimycotic and cultured at 37 °C under 5% CO_2 conditions.

4.3. Plasmids

The plasmid-encoding human ROS1 (ROS1-myc, #RC220652) was obtained from OriGene Technologies (Rockville, MD, USA). A fragment-encoding amino acid residue 1860–1882 (T), 1860–1894 (TP), 1883–2347 (PC), or 1895–2347 (C) of ROS1 was amplified from an ROS1-myc plasmid with PCR using primers for the T domain (forward: 5′-CGGCTAGCATGACAAGTT TCATACT-3′ and reverse: 5′-GACCGGTAGCCAGACAAAG-3′), TP domain (forward: 5′-CGGCTAG CATGACAAGTTTCATACT-3′ and reverse: 5′-GACCGGTA GTTCCTTGGCA-3′), PC domain (forward: 5′-CGGCTAGCATGCATAGAAGATTAAA-3′ and reverse: 5′-GACCGGTAGATCAGACCCATC-3′), or C domain (forward: 5′-CGGCTAGCATGGGGGTGACAGT-3′ and reverse: 5′-GACCGGTAG ATCAGACCCATC-3′) and then subcloned into pEGFP-C1 via the NheI/AgeI sites. Myc construct was a gift from Dr. Christin Carter-Su [32]. mCherry-DRP1 (#49152) and MFN2-YFP (#28010) was obtained from Addgene (Watertown, MA, USA). mCherry-DRP1 was subjected to PCR to introduce cleavage sites at the 5′ and 3′ ends of mCherry (forward: 5′-CGGATCCGGTCGCCACCATGGTGAG-3′ and reverse 5′-CGGACTTGTACAGCTCGTCCA-3′), and the PCR products were subcloned into MFN2-YFP via the BamHI/BsrGI sites to replace YFP and generate the MFN2-mcherry construct.

4.4. Knockdown of ROS1

pLKO.1-TRC2.Void [Scramble (Scr), ASN0000000001] and pLKO.1-shROS1 (TRCN0000219660) were obtained from the National Core Facility at the Institute of Molecular Biology, Genomic Research Center, Academic Sinica, Taiwan. Lentivirus containing pLKO.1-TRC2.Void or pLKO.1-shROS1 was prepared from 293T cells cotransfected with pCMVΔR8.91 and pMD.G along with pLKO.1-TRC2.Void or pLKO.1-shROS1. Medium containing lentivirus was harvested and added into OC3-IV2 cells. OC3-IV2 cells were subjected to selection with 2 μg/mL puromycin for at least 2 weeks.

4.5. Reverse Transcription and Semiquantitative Real-time PCR (Q-PCR)

RNA was isolated from OSCC cells using TRIzol reagent (Invitrogen) and converted to cDNA using a reverse transcription kit (Applied Biosystems, Foster City, CA, USA). Q-PCR was performed using the Power SYBR Green PCR Master Mix and ABI StepOnePlus Real-Time PCR System (Applied Biosystems) with specific primers: *ACTB* (forward: 5′-AGGATCTTCATGAGGTAGTCAGTCAG-3′ and reverse: 5′-CCACACTGTGCCCATCTACG-3′), *TERT* (forward: 5′-CAAGCACTTCCTCTACTCCTC-3′ and reverse: 5′-TGGAACCCAGAAAGATGGTC-3′), NRF1 (forward: 5′-GGCACTGTCTCACTTA TCCAGGTT-3′ and reverse: 5′-CAGCCACGGCAGAATAATTCA-3′), *PGC-1α* (forward: 5′-AATC AGACCTGACACAACAC-3′ and reverse: 5′-GCACTCCTCAATTTCACCAA-3′), *TFAM* (forward: 5′-ACTGCGCTCCCCCTTCAG-3′ and reverse: 5′-ACAGATGAAAACCACCTCGGTAA-3′), MT-CO1 (forward: 5′-GGCCTGACTGGCATTGTATT-3′ and reverse: 5′-TGGCGTAGGTTTGGTCTAGG-3′), *MT-CO2* (forward: 5′-CGATCCCTCCCTTACCATCA-3′ and reverse: 5′-CCGTAGTCGGTGTACTC GTAGGT-3′), *MT-ND1* (forward: 5′-CCAATGATGGCGCGATG-3′ and reverse: 5′-CTTTTTGG ACAGGTGGTGTGT-3′), *MT-ATP6* (forward: 5′-CCCACTTCTTACCACAAGGC-3′ and reverse: 5′-GT AGGTGGCCTGCAGTAATG-3′), *MT-CYTB* (forward: 5′-CTCCCGTGAGGCCAAATATC-3′ and reverse: 5′-GAATCGTGTGAGGGTGGGAC-3′), *IDH1* (forward: 5′-ATGCAAGGAGATGAAATGAC ACG-3′ and reverse: 5′-GCATCACGATTCTCTATGCCTAA-3′), *IDH2* (forward: 5′-TACGGGTCATC TCATCACCA-3′ and reverse: 5′-ACCTCGCAAGAGCAGCC-3′), *PFKP* (forward: 5′-CGGAG TTCCTGGAGCACCTCTC-3′ and reverse: 5′-AAGTACACCTTGGCCCCCACGTA-3′), *ACLY* (forward: 5′-GAAGGGAGTGACCATCATCG-3′ and reverse: 5′-TTAAAGCACCCAGGCTTGAT-3′), *OGDH* (forward: TCA-3′ and reverse: 5′-GGTTCAGTGAGCCCATGTCAA-3′), *PGK1* (forward: 5′-GGGCA AGGATGTTCTGTTCT-3′ and reverse: 5′-TC TCCAGCAGGATGACAGAC-3′), *PKM* (forward: 5′-ATC GTCCTCACCAAGTCTGG-3′ and reverse: 5′-GAAGATGCCACGGTACAGGT-3′), *LDHA* (forward: 5′-AGCCCGATTCCGTTACCT-3′ and reverse: 5′-CACCAGCAACATTCATTCCA-3′), *SLC2A1* (forward: 5′-CCAGCTGCCATTGCCGTT-3′ and reverse: 5′-GACGTAGGGACCACACAGTTGC-3′),

GLS1 (forward: 5′-TGGTGGCCTCAGGTGAAAAT-3′ and reverse: 5′-CCAAGCTAGGTAACAGAC CCTGTTT-3′), *ALDH1* (forward: 5′-GTTGTCAAACCAGCAGAGCA-3′ and reverse: 5′-AGGC CCATAACCAGGAACAA-3′), *SOX2* (forward: 5′-AGGATAAGTACACGCTGCCC-3′ and reverse: 5′-TTCATGTGCGCGTAACTGTC-3′), *IL13RA2* (forward: 5′-AGTTAAACCTTTGCCGCCAG-3′ and reverse: 5′-AGGTCCCAAAGGTATGCTCC-3′), and *GAPDH* (forward: 5′-CAAGGCTGTGGGCA AGGT-3′ and reverse: 5′-GGAAGGCCATGCCAGTGA-3′). All results of Q-PCR were normalized to *GAPDH*.

4.6. Immunoblotting

Cells were lysed in SDS lysis buffer (240 mM Tris-acetate, pH 7.8, 5 mM EDTA, 1% (*w/v*) SDS, 0.5% *(v/v)* glycerol) containing 1 mM sodium orthovanadate (Na_3VO_4), 1 mM phenylmethylsulfonyl fluoride, 10 ng/mL leupeptin, and 10 ng/mL aprotinin. Protein concentrations were determined by the bicinchoninic acid assay (Santa Cruz Biotechnology), and were separated by SDS-PAGE. The separated proteins were transferred to a membrane and immunoblotted with the primary antibodies indicated in each figure and the appropriate IRDye-conjugated secondary antibody. Immunopositive bands were detected using the Odyssey infrared imaging system (LI-COR Biosciences).

4.7. Immunofluorescence Staining, Confocal Microscopy, Mitochondrial Morphology, and Colocalization Analysis

For immunofluorescence staining, cells were fixed in 4% *(v/v)* paraformaldehyde and permeabilized in 0.1% Triton X-100. Cells were then incubated in a blocking buffer containing 1% bovine serum albumin and then with the indicated primary antibodies followed by Alexa Fluor–conjugated secondary antibodies. Nuclei were stained with 4′,6-diamidino-2-phenylindole (DAPI), and cells were mounted using Prolong Gold reagent (Invitrogen). Images were acquired using a LSM780 confocal microscope and analyzed with ZEN 2012 software (Zeiss, Jena, Germany). Mitochondrial morphology in cells was categorized into three different groups: tubular, fragmented, and intermediate. Tubular had at least one mitochondrial tubule ≥5 μm in length; intermediate, at least one between 2 and 5 μm, but no longer than 5 μm; fragmented, none ≥2 μm in length. Mitochondrial length was calculated using the Simple Neurite Tracer plugin of ImageJ software. For the colocalization analysis, the Colocalization Colormap plugin of ImageJ was used to generate a color-coded image of colocalization and calculate the normalized mean deviation product (nMDP) value and index of correlation (Icorr). The nMDP value represents the noncolocalization with cold colors (range −1 to 0) and colocalization with warm colors (range 0 to 1). Icorr indicated the fraction of positively correlated pixels in the image.

4.8. Subcellular Fractionation and Proteinase K Treatment of Mitochondria

Mitochondrial and cytoplasmic fractions were extracted using the Mitochondria Isolation Kit for Cultured Cells (Thermo Fisher Scientific, #89874, Waltham, MA, USA). Briefly, cells were collected and then incubated with Reagent A for 2 min on ice. Reagent B was added, and the sample was vortexed at maximum speed, followed by incubation for 5 min on ice. Reagent C was added, and the sample was centrifuged at 700× *g* at 4 °C for 10 min. The supernatant was collected and centrifuged at 12,000× *g* at 4 °C for 15 min. The supernatant represented the cytoplasmic fraction, and the pellet represented the mitochondria-enriched fraction. The pellet was washed using Reagent C and then lysed with SDS lysis buffer. For digestion with proteinase K, equivalent weights of the mitochondria-enriched fraction were resuspended in digestion buffer (250 mM sucrose, 0.5 mM EGTA, 0.5 mM EDTA, 3 mM HEPES-NaOH, pH 7.2), and proteinase K (Sigma-Aldrich) was added to a final concentration of 0.25, 0.5, 1, or 2 μg/mL with or without 1% *(v/v)* Triton X-100, with incubation for 20 min on ice. The reaction was stopped by the addition of 2 mM phenylmethylsulfonyl fluoride, and samples were collected and lysed after centrifugation at 15,000× *g* at 4 °C for 10 min.

4.9. Measurement of Oxygen Consumption Rate (OCR)

The OCRs were measured using the Seahorse XF24 Analyzer (Taiwan Mitochondrion Applied Technology, Taiwan). Cells were seeded at 1.7×10^4 per well in DMEM/keratinocyte serum-free medium containing 10% *(v/v)* fetal bovine serum. After 24 h, cells were transferred into assay media and subjected to addition of either 1 μM oligomycin, 1 μM FCCP, 1 μM rotenone, or 1 μM antimycin A, for determination of basal OCR, ATP production, maximal OCR, and spare respiratory capacity, respectively.

4.10. Statistical Analysis

Statistical analysis of all results was carried out using the paired Student's *t*-test. All values reflect the mean ± SEM of data obtained from at least three independent experiments, if not otherwise specified. Significance was defined as $p < 0.05$.

5. Conclusions

In summary, our results demonstrate that oncogenic ROS1 is present in mitochondria, governs mitochondrial morphogenesis, and confers metabolic plasticity to promote oral cancer invasiveness. Therefore, targeting mitochondrial ROS1 may provide a new therapeutic approach for treating OSCC and prevention of OSCC metastasis.

Supplementary Materials: The following are available online at http://www.mdpi.com/2072-6694/12/10/2845/s1, Figure S1: Distribution of ROS1 mutants and their effects on mitochondrial phenotype in COS7 cells, Figure S2: ROS1 oncoprotein does not interact with DRP1 or MFN2, Figure S3: Comparison of stemness gene expression in OSCC cells, Figure S4: Full images of the western blot analysis for Figure 1, Figure S5: Full images of the western blot analysis for Figure 2.

Author Contributions: Conceptualization, L.C. and Y.-J.C.; Methodology, Y.-J.C. and K.-W.C.; Validation, Y.-J.C.; Formal analysis, Y.-J.C.; Investigation, L.C. and Y.-J.C.; Resources, L.C. and Y.-J.C.; Data curation, Y.-J.C. and K.-W.C.; Writing—original draft, L.C. and Y.-J.C.; Writing—review and editing, L.C., Y.-J.C., K.-W.C.; Visualization, Y.-J.C.; Supervision, L.C.; Project administration, L.C. and Y.-J.C.; Funding acquisition, L.C. and Y.-J.C. All authors have read and agreed to the published version of the manuscript.

Funding: This work was supported by grants from the Ministry of Science and Technology, Taiwan (Grant # MOST 106-2321-B-007-007-MY3 to Y.-J.C. and 105-2320-B-007-002-MY3 to L.C.).

Conflicts of Interest: The authors declare no conflict of interest.

References

1. Godeny, M. Prognostic factors in advanced pharyngeal and oral cavity cancer; significance of multimodality imaging in terms of 7th edition of TNM. *Cancer Imaging* **2014**, *14*, 15. [CrossRef] [PubMed]
2. Loeffler-Ragg, J.; Schwentner, I.; Sprinzl, G.M.; Zwierzina, H. EGFR inhibition as a therapy for head and neck squamous cell carcinoma. *Expert Opin. Investig. Drugs* **2008**, *17*, 1517–1531. [CrossRef] [PubMed]
3. Bonner, J.A.; Harari, P.M.; Giralt, J.; Azarnia, N.; Shin, D.M.; Cohen, R.B.; Jones, C.U.; Sur, R.; Raben, D.; Jassem, J.; et al. Radiotherapy plus cetuximab for squamous-cell carcinoma of the head and neck. *N. Engl. J. Med.* **2006**, *354*, 567–578. [CrossRef] [PubMed]
4. Vermorken, J.B.; Mesia, R.; Rivera, F.; Remenar, E.; Kawecki, A.; Rottey, S.; Erfan, J.; Zabolotnyy, D.; Kienzer, H.R.; Cupissol, D.; et al. Platinum-based chemotherapy plus cetuximab in head and neck cancer. *N. Engl. J. Med.* **2008**, *359*, 1116–1127. [CrossRef] [PubMed]
5. Vermorken, J.B.; Trigo, J.; Hitt, R.; Koralewski, P.; Diaz-Rubio, E.; Rolland, F.; Knecht, R.; Amellal, N.; Schueler, A.; Baselga, J. Open-label, uncontrolled, multicenter phase II study to evaluate the efficacy and toxicity of cetuximab as a single agent in patients with recurrent and/or metastatic squamous cell carcinoma of the head and neck who failed to respond to platinum-based therapy. *J. Clin. Oncol. Off. J. Am. Soc. Clin. Oncol.* **2007**, *25*, 2171–2177. [CrossRef]
6. Geva, Y.; Schuldiner, M. The back and forth of cargo exit from the endoplasmic reticulum. *Curr. Biol. CB* **2014**, *24*, R130–R136. [CrossRef]

7. Shih, C.H.; Chang, Y.J.; Huang, W.C.; Jang, T.H.; Kung, H.J.; Wang, W.C.; Yang, M.H.; Lin, M.C.; Huang, S.F.; Chou, S.W.; et al. EZH2-mediated upregulation of ROS1 oncogene promotes oral cancer metastasis. *Oncogene* **2017**, *36*, 6542–6554. [CrossRef]
8. Huang, W.C.; Chan, S.H.; Jang, T.H.; Chang, J.W.; Ko, Y.C.; Yen, T.C.; Chiang, S.L.; Chiang, W.F.; Shieh, T.Y.; Liao, C.T.; et al. miRNA-491-5p and GIT1 serve as modulators and biomarkers for oral squamous cell carcinoma invasion and metastasis. *Cancer Res.* **2014**, *74*, 751–764. [CrossRef]
9. Davies, K.D.; Doebele, R.C. Molecular pathways: ROS1 fusion proteins in cancer. *Clin. Cancer Res. Off. J. Am. Assoc. Cancer Res.* **2013**, *19*, 4040–4045. [CrossRef]
10. Acquaviva, J.; Wong, R.; Charest, A. The multifaceted roles of the receptor tyrosine kinase ROS in development and cancer. *Biochim. Biophys. Acta* **2009**, *1795*, 37–52. [CrossRef]
11. Charest, A.; Kheifets, V.; Park, J.; Lane, K.; McMahon, K.; Nutt, C.L.; Housman, D. Oncogenic targeting of an activated tyrosine kinase to the Golgi apparatus in a glioblastoma. *Proc. Natl. Acad. Sci. USA* **2003**, *100*, 916–921. [CrossRef] [PubMed]
12. Neel, D.S.; Allegakoen, D.V.; Olivas, V.; Mayekar, M.K.; Hemmati, G.; Chatterjee, N.; Blakely, C.M.; McCoach, C.E.; Rotow, J.K.; Le, A.; et al. Differential Subcellular Localization Regulates Oncogenic Signaling by ROS1 Kinase Fusion Proteins. *Cancer Res.* **2019**, *79*, 546–556. [CrossRef] [PubMed]
13. Cheng, Y.; Sun, Y.; Wang, L.Z.; Yu, Y.C.; Ding, X. Cytoplasmic c-ros oncogene 1 receptor tyrosine kinase expression may be associated with the development of human oral squamous cell carcinoma. *Oncol. Lett.* **2015**, *10*, 934–940. [CrossRef] [PubMed]
14. Lee, J.; Kim, D.H.; Hwang, I. Specific targeting of proteins to outer envelope membranes of endosymbiotic organelles, chloroplasts, and mitochondria. *Front. Plant Sci.* **2014**, *5*, 173. [CrossRef]
15. Zhao, J.; Zhang, J.; Yu, M.; Xie, Y.; Huang, Y.; Wolff, D.W.; Abel, P.W.; Tu, Y. Mitochondrial dynamics regulates migration and invasion of breast cancer cells. *Oncogene* **2013**, *32*, 4814–4824. [CrossRef]
16. Ma, J.T.; Zhang, X.Y.; Cao, R.; Sun, L.; Jing, W.; Zhao, J.Z.; Zhang, S.L.; Huang, L.T.; Han, C.B. Effects of Dynamin-related Protein 1 Regulated Mitochondrial Dynamic Changes on Invasion and Metastasis of Lung Cancer Cells. *J. Cancer* **2019**, *10*, 4045–4053. [CrossRef]
17. Mishra, P.; Chan, D.C. Metabolic regulation of mitochondrial dynamics. *J. Cell Biol.* **2016**, *212*, 379–387. [CrossRef]
18. Cannino, G.; Ciscato, F.; Masgras, I.; Sanchez-Martin, C.; Rasola, A. Metabolic Plasticity of Tumor Cell Mitochondria. *Front. Oncol.* **2018**, *8*, 333. [CrossRef]
19. Kim, J.W.; Dang, C.V. Cancer's molecular sweet tooth and the Warburg effect. *Cancer Res.* **2006**, *66*, 8927–8930. [CrossRef]
20. Lehuede, C.; Dupuy, F.; Rabinovitch, R.; Jones, R.G.; Siegel, P.M. Metabolic Plasticity as a Determinant of Tumor Growth and Metastasis. *Cancer Res.* **2016**, *76*, 5201–5208. [CrossRef]
21. Kashatus, J.A.; Nascimento, A.; Myers, L.J.; Sher, A.; Byrne, F.L.; Hoehn, K.L.; Counter, C.M.; Kashatus, D.F. Erk2 phosphorylation of Drp1 promotes mitochondrial fission and MAPK-driven tumor growth. *Mol. Cell* **2015**, *57*, 537–551. [CrossRef] [PubMed]
22. Kim, D.I.; Lee, K.H.; Gabr, A.A.; Choi, G.E.; Kim, J.S.; Ko, S.H.; Han, H.J. Abeta-Induced Drp1 phosphorylation through Akt activation promotes excessive mitochondrial fission leading to neuronal apoptosis. *Biochim. Biophys. Acta* **2016**, *1863*, 2820–2834. [CrossRef] [PubMed]
23. Gao, S.; Li, H.; Cai, Y.; Ye, J.T.; Liu, Z.P.; Lu, J.; Huang, X.Y.; Feng, X.J.; Gao, H.; Chen, S.R.; et al. Mitochondrial binding of alpha-enolase stabilizes mitochondrial membrane: Its role in doxorubicin-induced cardiomyocyte apoptosis. *Arch. Biochem. Biophys.* **2014**, *542*, 46–55. [CrossRef]
24. Kim, Y.M.; Youn, S.W.; Sudhahar, V.; Das, A.; Chandhri, R.; Cuervo Grajal, H.; Kweon, J.; Leanhart, S.; He, L.; Toth, P.T.; et al. Redox Regulation of Mitochondrial Fission Protein Drp1 by Protein Disulfide Isomerase Limits Endothelial Senescence. *Cell Rep.* **2018**, *23*, 3565–3578. [CrossRef] [PubMed]
25. Wang, Y.N.; Hung, M.C. Nuclear functions and subcellular trafficking mechanisms of the epidermal growth factor receptor family. *Cell Biosci.* **2012**, *2*, 13. [CrossRef]
26. Demory, M.L.; Boerner, J.L.; Davidson, R.; Faust, W.; Miyake, T.; Lee, I.; Huttemann, M.; Douglas, R.; Haddad, G.; Parsons, S.J. Epidermal growth factor receptor translocation to the mitochondria: Regulation and effect. *J. Chem.* **2009**, *284*, 36592–36604. [CrossRef]

27. Che, T.F.; Lin, C.W.; Wu, Y.Y.; Chen, Y.J.; Han, C.L.; Chang, Y.L.; Wu, C.T.; Hsiao, T.H.; Hong, T.M.; Yang, P.C. Mitochondrial translocation of EGFR regulates mitochondria dynamics and promotes metastasis in NSCLC. *Oncotarget* **2015**, *6*, 37349–37366. [CrossRef]
28. Chen, M.K.; Hung, M.C. Proteolytic cleavage, trafficking, and functions of nuclear receptor tyrosine kinases. *FEBS J.* **2015**, *282*, 3693–3721. [CrossRef]
29. Peiris-Pages, M.; Bonuccelli, G.; Sotgia, F.; Lisanti, M.P. Mitochondrial fission as a driver of stemness in tumor cells: mDIVI1 inhibits mitochondrial function, cell migration and cancer stem cell (CSC) signalling. *Oncotarget* **2018**, *9*, 13254–13275. [CrossRef]
30. Lin, S.C.; Liu, C.J.; Chiu, C.P.; Chang, S.M.; Lu, S.Y.; Chen, Y.J. Establishment of OC3 oral carcinoma cell line and identification of NF-kappa B activation responses to areca nut extract. *J. Oral Pathol. Med.* **2004**, *33*, 79–86. [CrossRef]
31. Lu, Y.C.; Chen, Y.J.; Wang, H.M.; Tsai, C.Y.; Chen, W.H.; Huang, Y.C.; Fan, K.H.; Tsai, C.N.; Huang, S.F.; Kang, C.J.; et al. Oncogenic function and early detection potential of miRNA-10b in oral cancer as identified by microRNA profiling. *Cancer Prev. Res.* **2012**, *5*, 665–674. [CrossRef] [PubMed]
32. Rui, L.; Herrington, J.; Carter-Su, C. SH2-B is required for nerve growth factor-induced neuronal differentiation. *J. Biol. Chem.* **1999**, *274*, 10590–10594. [CrossRef] [PubMed]